A Compliant and Redundantly Actuated 3-DOF 4RRR PKM: First Step to Full Planar Motion

Paul Stoffels, Ronald Aarts

Applied Mechanics & Data Analysis
Faculty of Engineering Technology
University of Twente
P.O. Box 217, 7500 AE Enschede, The Netherlands
paul.stoffels96@gmail.com, r.g.k.m.aarts@utwente.nl

ABSTRACT

The development and optimisation of compliant (or flexure-based) manipulators with redundant actuation have been considered before, showing that the redundancy can be exploited to increase the support stiffness and reduce actuator loads. However, so far only 2-DOF manipulators have been considered which enable translational motion in two directions. In this paper a third degree of freedom, the in-plane rotation of the end effector, is added. The goal is to design and evaluate a first prototype capable of full planar motion. The dynamic performance of the manipulator is analysed with a flexible multibody model. The links are assumed to be rigid. The SPACAR software is used as its flexible beam element can describe the non-linear behaviour of the flexure joints well at rather large deflections and accounts for constraint warping. In this prototype the end effector range of motion is limited such that the joint rotations do not exceed $\pm 30°$. Butterfly and cartwheel flexure joints can handle the specifications without violating stress constraints. In the final design the lowest natural frequencies are 3.6 Hz for both translations and 7.9 Hz for the rotation. The first parasitic frequency is expected at 76 Hz, which is sufficiently high. This prototype has been manufactured with 3D printing. The lowest translational frequencies appear to be somewhat higher than expected, which could arise from stiffness added by the flexible coupling between actuator and upper arm. A higher resonance frequency is found near 80 Hz, which agrees well with the expected first relevant parasitic mode.

Keywords: Flexure-based mechanisms, Redundantly actuated parallel kinematic manipulator (PKM), Non-linear beam elements, Experimental system identification.

1 INTRODUCTION

In [1, 2] compliant and redundantly actuated 2-DOF 3RRR parallel kinematic manipulators (PKM) have been introduced and optimised as "best of both worlds" for precision applications. Being compliant mechanisms, or more precisely flexure-based mechanisms, deterministic behaviour can be realised because of the low level of friction, hysteresis and backlash [3, 4]. Being also a redundantly actuated PKM, it combines the advantages of PKM, i.e. higher stiffness, low inertia and large accelerations, with an improved handling of singularities and optimised actuator loading made possible by the redundancy [5, 6, 7, 8].

Simulations and experimental tests indeed demonstrated advantages of combining both concepts [1]. However a drawback of the developed 2-DOF prototype is the limitation to only translational motion. Hence, in this paper a third degree of freedom is added which is the in-plane rotation of the end effector. The design considerations, methodology and results will be presented for the first prototype capable of full planar motion shown in Fig. 1(a) and detailed in the following sections.

2 CONCEPTUAL DESIGN

This first prototype of the planar 3-DOF 4RRR PKM with compliant joints is mainly realised to understand the relevant steps in the dynamic modelling, design optimisation and control. Hence, it

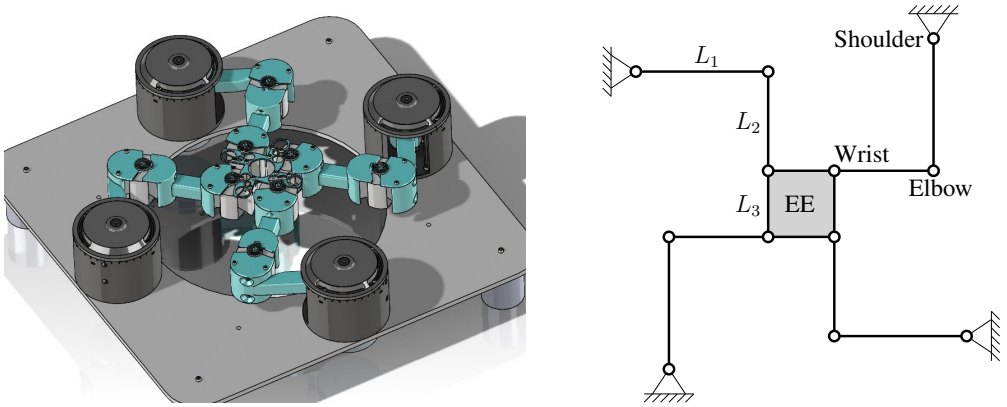

(a) CAD drawing [9]. (b) Manipulator schematic top view.

Figure 1. Design of the planar 3-DOF 4RRR PKM with compliant joints.

is not needed to aim for a highly optimised performance. Instead the design freedom is limited such that the optimisation gives results and insight in a reasonable time. The main design considerations are given in this section to define the system to be analysed in the next sections.

2.1 Arm lengths and system dimensions

The four arms of the 4RRR PKM are assumed to be similar and the actuators are located at the corners of a square. Fig. 1(b) shows a simplified kinematic model in which the shoulder, elbow and wrist joints are assumed to be ideal revolute joints. Characteristic dimensions are lengths L_1 and L_2 of upper and lower arm, respectively, as well as length L_3 that represents the dimension of the rigid square end effector (EE). All lengths can be chosen independently, where in particular the total length $L_1 + L_2$ of a fully stretched arm can be split arbitrarily into both contributions L_1 and L_2. In the previous studies [1, 2] no advantage was found for different lengths of upper and lower arm and hence these lengths are taken equal, i.e. $L_1 = L_2$.

Length L_3 defines the dimension of the end effector. Having a large end effector is favourable from a kinematic view as it allows better control of the EE rotation which follows directly from the differences between the positions of the wrist joints divided by L_3. However, a large L_3 results in a bulky and heavy end effector which negatively affects the dynamic performance. Hence, L_3 is chosen not too large, but sufficiently large to avoid collisions of the flexures of the wrist joints.

The overall dimensions of the system follow from the distance R between the actuator locations and the centre of the end effector in the presented neutral configuration. Similar to the previous designs $R = 230.5$ mm [1, 2].

2.2 Flexure joint types

For this first prototype the effective workspace of the manipulator has been limited to avoid rotations larger than $\pm 30^\circ$ in all flexure joints. From the simplified model in Fig. 1(b) it can be understood quite straightforwardly that a rotation of the end effector results in about the same rotation of the wrist joints. To allow combined rotation and translation of the end effector, its rotation is limited to $\pm 15^\circ$. Butterfly flexure joints [10], see Fig. 2(b), can handle large rotations up to $\pm 30^\circ$ without a significant loss of support stiffness and are therefore used for the elbow and wrist joints. To enable these joint rotations, the angle between the leaf springs is chosen accordingly as shown in the figure.

For the specified EE motion it is expected that the shoulder only has to rotate about $\pm 15^\circ$. In this smaller range a cartwheel flexure joint, see Fig. 2(a), can offer higher, or at least comparable, support stiffness compared to the butterfly flexure joint. Hence cartwheel flexure joints are used for the shoulder joints because of their lower complexity.

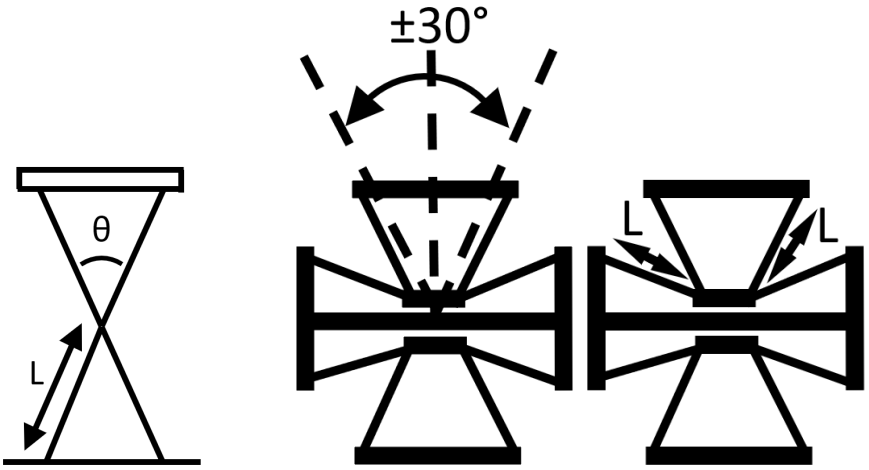

(a) Cartwheel flexure. (b) Butterfly flexure.

Figure 2. Flexure joint types with two design parameters: The angle θ between the leaf springs and the length L of one leaf spring [9].

2.3 Actuators and sensors

The manipulator is driven by rotational actuators that are mounted at the shoulders. The actuators are direct drive Maxon EC 90 flat brushless motors (part number 323772, nominal torque 0.444 Nm), equipped with a co-located MILE encoder (part number 411966, 6400 pulses/revolution, so 25600 counts/revolution when used as a quadrature encoder). The motor axle is connected to the upper arm with a flexible coupling (SICK KUP-1010-B), which allows for a maximum misalignment of 0.3 mm.

2.4 Manufacturing and material

The links and joints are manufactured with 3D printing. For the arms relatively low-cost Fused Deposition Modeling (FDM) of PLA is adequate. The joints are produced with Selective Laser Sintering (SLS) of Nylon (PA2200) that can meet stricter geometric tolerances. The relevant material properties are listed in Table 1.

Table 1. Material properties.

Material	Property	Value	Unit
PolyLactic Acid (PLA) [11]	Tensile strength	59	MPa
	Young's modulus	3.5	GPa
	Density	1252	kg/m^3
Nylon PA2200 [12]	Tensile strength	45	MPa
	Young's modulus	1.7	GPa
	Density	930	kg/m^3

3 NUMERICAL MODEL

To analyse and optimise the manipulator design, two types of models have been used as will be detailed in this section. First a low order model is considered that only accounts for the intended motion in the three degrees of freedom of the end effector. Next a more complicated flexible multibody model is needed to analyse e.g. the finite support stiffness.

3.1 3-DOF dynamic model

A low order 3-DOF model is derived first. It should capture the main low frequent dynamic behaviour, i.e. to evaluate the three lowest natural frequencies and the required actuator torques. This simplified model follows from Fig. 1(b) where the ideal revolute joints are assumed with a constant compliance for the in-plane rotation and infinite stiffness in all other directions. With these assumptions, the velocities of the links and the relative rotations of the joints can be expressed in the position, rotation and (angular) velocities of the end effector. Knowing these kinematic relations, the (link) masses and the (joint) rotational stiffnesses, the low order model can be obtained relatively straightforwardly e.g. using the Euler-Lagrange equation. The result can be expressed in the usual way as

$$\bar{\mathbf{M}}(\mathbf{q})\ddot{\mathbf{q}} + \mathbf{C}(\mathbf{q},\dot{\mathbf{q}})\dot{\mathbf{q}} + \mathbf{Q}(\mathbf{q}) = \mathbf{A}^T(\mathbf{q})\boldsymbol{\tau}, \tag{1}$$

where $\mathbf{q}$ are the three independent coordinates for which it is convenient to take the EE Cartesian coordinates x_{ee}, y_{ee} and its rotation θ_{ee}. Matrix $\bar{\mathbf{M}}$ is the configuration dependent (reduced) mass matrix; $\mathbf{C}$ accounts for the Coriolis terms; $\mathbf{Q}$ represents the (non-linear) stiffness contributions and the transpose of the Jacobian matrix $\mathbf{A}$ transforms the vector $\boldsymbol{\tau}$ with four actuator torques τ_i ($i = 1..4$) into effective forces $f_{x,ee}$, $f_{y,ee}$ and torque τ_{ee} on the end effector.

3.2 Redundant actuation

The non-square Jacobian matrix $\mathbf{A}$ in Eq. (1) reflects the redundant actuation which means that there is not a unique solution for the actuator torques τ_i ($i = 1..4$) for a specified effective end effector force and torque

$$\begin{bmatrix} f_{x,ee} \\ f_{y,ee} \\ \tau_{ee} \end{bmatrix} = \mathbf{A}^T(\mathbf{q}) \begin{bmatrix} \tau_1 \\ \tau_2 \\ \tau_3 \\ \tau_4 \end{bmatrix}. \tag{2}$$

All possible solutions for the actuator torques can be written as

$$\begin{bmatrix} \tau_1 \\ \tau_2 \\ \tau_3 \\ \tau_4 \end{bmatrix} = \left(\mathbf{A}^T(\mathbf{q})\right)^\dagger \begin{bmatrix} f_{x,ee} \\ f_{y,ee} \\ \tau_{ee} \end{bmatrix} + \lambda \ \mathrm{null}(\mathbf{A}^T), \tag{3}$$

where $(\mathbf{A}^T(\mathbf{q}))^\dagger$ is the Moore–Penrose pseudo-inverse of $\mathbf{A}^T$, $\mathrm{null}(\mathbf{A}^T)$ refers to the null space of the matrix, which is a vector, and scalar λ can be chosen arbitrarily. Several optimal solutions can be considered. The 2-norm minimises the length of vector $\boldsymbol{\tau}$. This solution is found straightforwardly taking $\lambda = 0$ in Eq. (3).

Alternatively, the ∞-norm minimises the maximum absolute value of the four actuator torques, which may be more beneficial to avoid actuator saturation in case of limited maximum actuator torque. This solution can be found graphically from Fig. 3. This figure gives an example of how the absolute values of the actuator torques can vary as functions of λ. According to Eq. (3) linear relations are found where the respective slopes of the lines follow from the null space. Following the algorithm proposed by Woo *et al.* [13] the optimum according to the ∞-norm is found as the lowest intersection of the lines with the largest torques, i.e. the solid dot where (in this example) $|\tau_2| = |\tau_4|$. Note that this solution is close to the 2-norm optimal solution with $\lambda = 0$.

3.3 Redundant sensing

Fig. 4 clarifies the redundant sensing of the manipulator. The co-located encoders measure the four shoulder angles $\phi_{1,4,7,10}$ from which the three EE coordinates $\mathbf{q} = [x_{ee}, y_{ee}, \theta_{ee}]^T$ should be computed. The excess of one sensor indicates the redundancy as four equations can be derived for the three EE coordinates as follows.

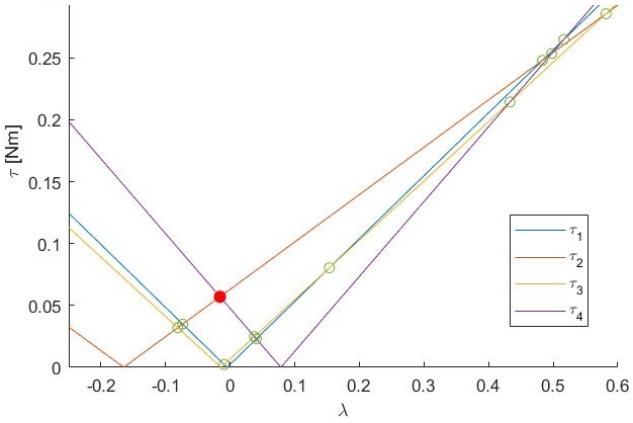

Figure 3. Examples of the absolute torques that are solutions of Eq. (3) for an arbitrary Jacobian matrix $\mathbf{A}^T$.

The positions of the elbow joints $(x_{2,5,8,11}, y_{2,5,8,11})$ follow directly from the (fixed) shoulder positions, the shoulder angles $\phi_{1,4,7,10}$ and upper arm lengths L_1. Similarly, the positions of the wrist joints $(x_{3,6,9,12}, y_{3,6,9,12})$ can be expressed in the (unknown) EE coordinates $\mathbf{q}$ and the EE dimension L_3. Then four constraint equations have to be satisfied for the lower arms

$$\mathbf{S}(\mathbf{q}) = \begin{bmatrix} (x_3(\mathbf{q}) - x_2(\phi_1))^2 + (y_3(\mathbf{q}) - y_2(\phi_1))^2 - L_2^2 \\ (x_6(\mathbf{q}) - x_5(\phi_4))^2 + (y_6(\mathbf{q}) - y_5(\phi_4))^2 - L_2^2 \\ (x_9(\mathbf{q}) - x_8(\phi_7))^2 + (y_9(\mathbf{q}) - y_8(\phi_7))^2 - L_2^2 \\ (x_{12}(\mathbf{q}) - x_{11}(\phi_{10}))^2 + (y_{12}(\mathbf{q}) - y_{11}(\phi_{10}))^2 - L_2^2 \end{bmatrix} = 0. \tag{4}$$

In general no solution exists for $\mathbf{q}$ that exactly solves all four equations, but instead a minimal least squares solution can be obtained for these non-linear functions of $\mathbf{q}$. For a numerical solution the iterative Newton–Raphson method is well-suited. Knowing an estimate $\mathbf{q}^{(i)}$ for this solution, the next estimate $\mathbf{q}^{(i+1)}$ is computed with

$$\mathbf{q}^{(i+1)} = \mathbf{q}^{(i)} - \left(\mathbf{S}_{,\mathbf{q}}(\mathbf{q}^{(i)})\right)^{\dagger} \mathbf{S}(\mathbf{q}^{(i)}), \tag{5}$$

where $(\mathbf{S}_{,\mathbf{q}}(\mathbf{q}^{(i)}))^{\dagger}$ is the pseudo-inverse of the Jacobian of the constraint equations. The iterations can be continued until some preset accuracy is met. During real-time control, a finite amount

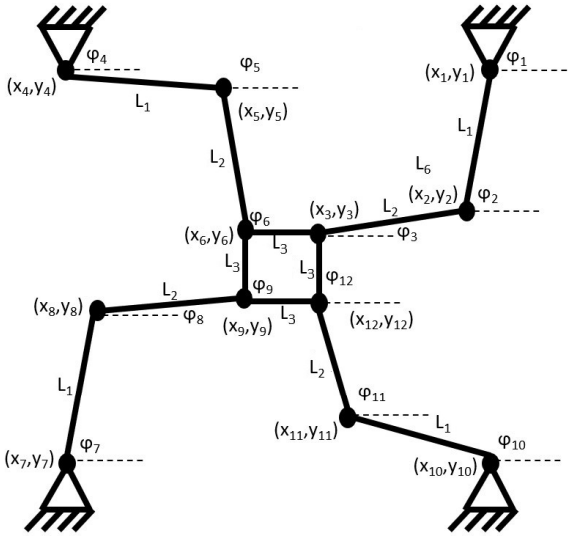

Figure 4. Schematic view of the manipulator including coordinates.

of time is available to perform calculations and then only a limited number of Newton-Raphson iterations can be executed. With sufficiently small time steps, the changes in all positions are quite small and typically a single iteration suffices.

3.4 Flexible multibody model and design optimisation

For design optimisation higher natural frequencies associated with unwanted parasitic vibrations must be known as well. Such higher order dynamic behaviour is investigated with a more advanced flexible multibody model in which all flexures are modelled in the SPACAR software package with non-linear beam elements that account for constraint warping [14].

Although this model can evaluate the natural frequencies throughout the manipulator workspace quite efficiently, a system level optimisation with many (geometric) parameters would still be quite involved. Instead, the design is optimised in parts. At first the length L and angle θ of the cartwheel flexure, see Fig. 2(a), are optimised for a high compliance of the in-plane rotation and a high parasitic natural frequency. Next the geometry of the butterfly hinges is determined. Finally, the arm lengths are chosen to obtain acceptable rotations for the shoulder joint.

4 NUMERICAL RESULTS

The dynamic properties of the complete manipulator are analysed with the advanced flexible multibody model. Fig. 5 shows the relevant natural frequencies and mode shapes in the neutral configuration. The natural frequencies of both in-plane translational modes are identical because of the symmetry and are low (3.6 Hz) which confirms the desired high compliance. The natural frequency of the in-plane rotational mode is acceptable as well (7.9 Hz). Next eight modes with a natural frequency of about 53 Hz represent internal modes in the butterfly flexures. For the pro-

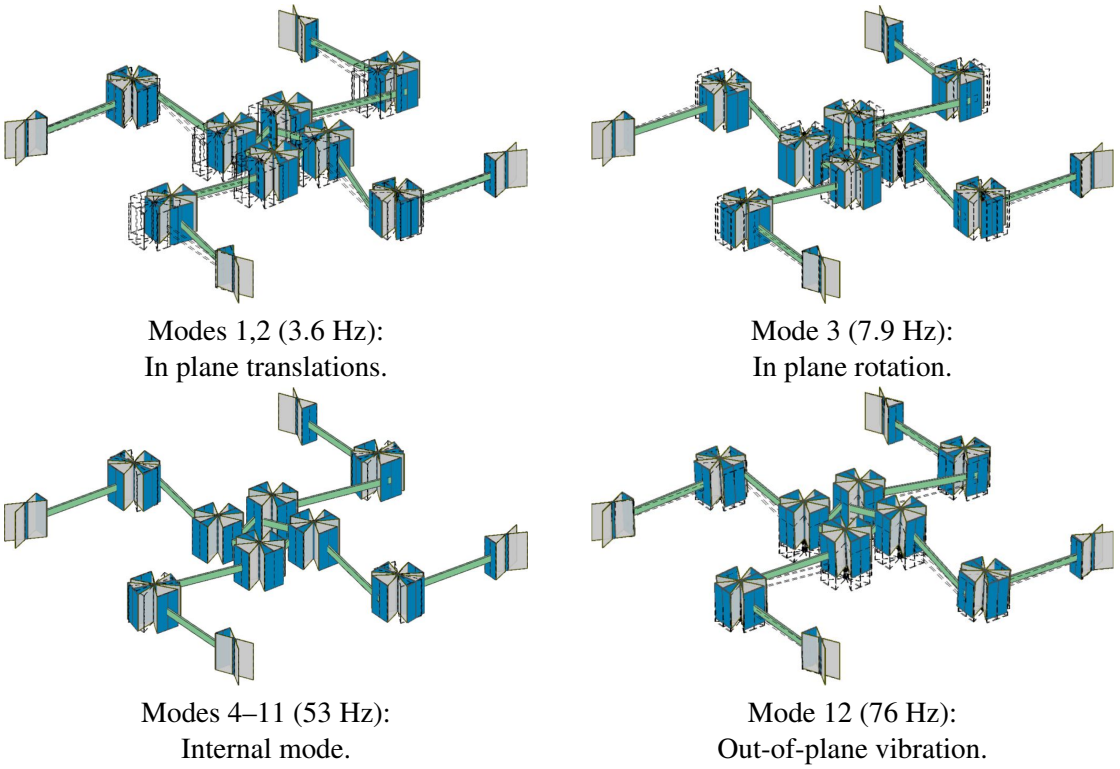

Figure 5. Natural frequencies and mode shapes of the 3-DOF 4RRR PKM with compliant joints. The "free" ends of the cartwheel flexures are in fact connected to the mounts (not shown).

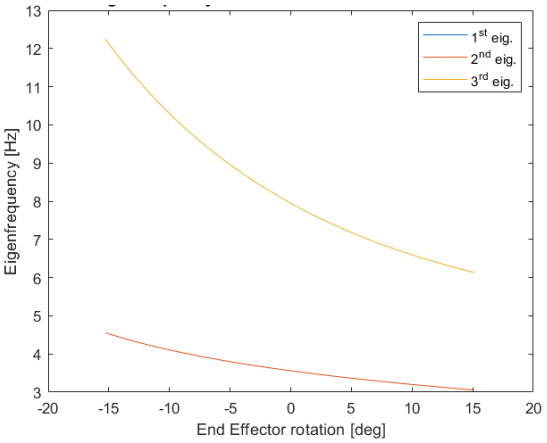

Figure 6. Natural frequencies of the system during EE rotation with $(x_{ee}, y_{ee}) = (0,0)$.

totype manipulator these modes are ignored. The next mode 12 is an out-of-plane vibration of the end effector and is expected to be the performance limiting first parasitic mode. Its natural frequency of 76 Hz is about an order larger than the three lowest natural frequencies, which is an acceptable result.

These natural frequencies and mode shape are found in the neutral position of the end effector, but will vary when it moves or rotates. Fig. 6 shows the variation of the lowest three natural frequency when the end effector rotates in the neutral position $(x_{ee}, y_{ee}) = (0,0)$. The first and second natural frequencies is are identical and show an asymmetric behaviour that is quite different for negative and positive EE rotation: It drops from 3.6 Hz to 3.1 Hz for $\theta_{ee} = +15°$, and increases to 4.5 Hz for $\theta_{ee} = -15°$. The third natural frequency shows a similar behaviour and varies between 6.1 Hz and 12.2 Hz. This variation is mainly caused by the change in mass matrix. Since the third natural frequency represents the rotation of the EE, this change in mass matrix means a change in inertia, which is obvious as the positions of the arms differ significantly comparing the configurations of EE rotations of $-15°$ and $+15°$.

Similarly the natural frequencies can also be investigated for linear displacements of the end effector. Fig. 7 presents the variation of the first natural frequency for fixed EE rotations of $-15°$ and $+15°$. The black curve in these figures indicates the border of the workspace that follows

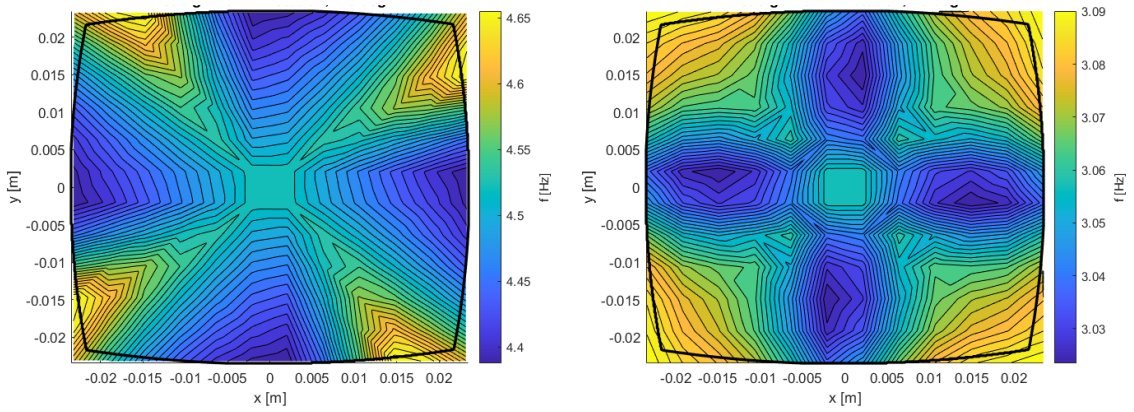

(a) EE rotation of $-15°$ (b) EE rotation of $+15°$

Figure 7. First natural frequency of the system with EE rotations of $-15°$ and $+15°$.

from the joint rotation limits. It appears that the natural frequencies depend only weakly on the position. Similar results are found for the second and third natural frequency. Note that for such displacements where the end effector is not in the neutral position, the symmetry of the system is broken such that the first and second natural frequencies are no longer equal.

5 EXPERIMENTAL RESULTS

Fig. 8 shows the diagonal parts of the experimentally identified Bode magnitude plot of the system in the neutral configuration. It is obtained by exciting the system with multi-sine signals in the frequency range from 1 Hz to 100 Hz. The lowest translational frequencies appear to be about 5 Hz which is somewhat higher than expected. This could be caused by the stiffness of the flexible coupling between actuator and upper arm which results in a higher stiffness compared to the model.

The internal mode of the butterfly flexures is not visible in the responses which justifies that these modes may be ignored during the design optimisation. The resonance frequency near 80 Hz agrees well with the expected frequency of the first relevant parasitic mode.

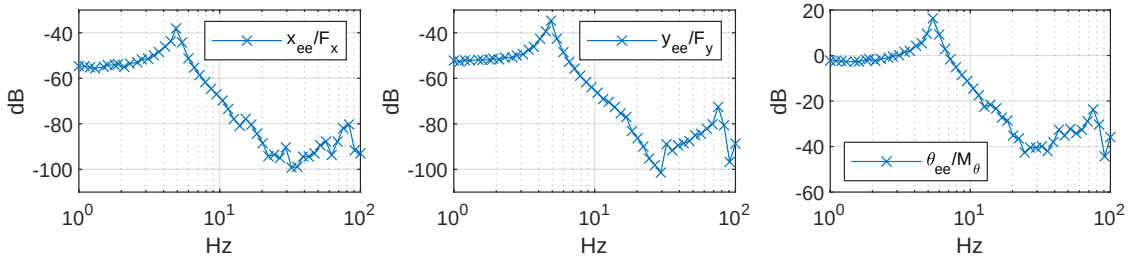

Figure 8. Diagonal parts of the experimental Bode magnitude plot of the system in the neutral configuration.

Unfortunately it appeared that the end effector could not move throughout the workspace as planned due to an obstruction of some parts. Nevertheless, the varying dynamic behaviour has been examined for a range end effector positions and rotations that can be realised.

Fig. 9(a) shows the Bode diagrams for the relation between x_{ee} and $f_{x,ee}$ with varying end effector rotations between $-5°$ and $0°$. It can be seen that the first natural frequency as well as the equivalent stiffness decrease when the end effector rotates in negative direction. This is presented in more detail in Fig. 10 which also includes the behaviour for rotations in the positive direction. Different from the expected behaviour, Fig. 6, the natural frequencies decrease for rotations in both positive and negative directions.

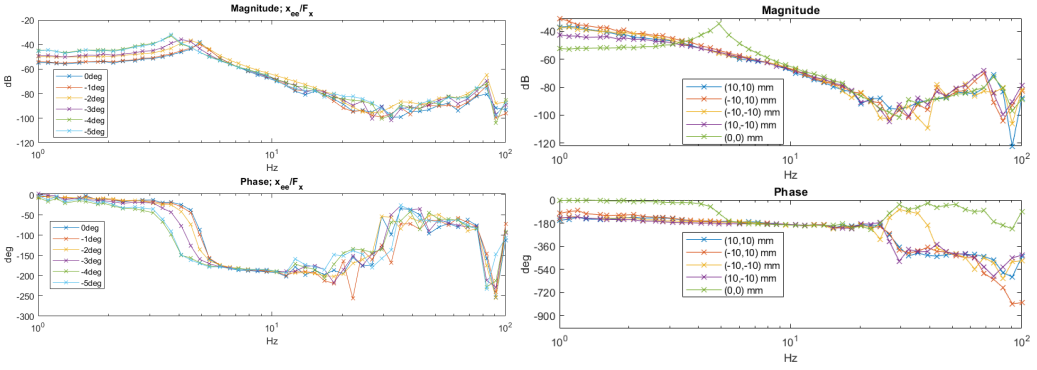

(a) $x_{ee}/f_{x,ee}$ for negative EE rotation (b) $y_{ee}/f_{y,ee}$ for EE linear displacement

Figure 9. Bode diagrams outside the neutral configuration.

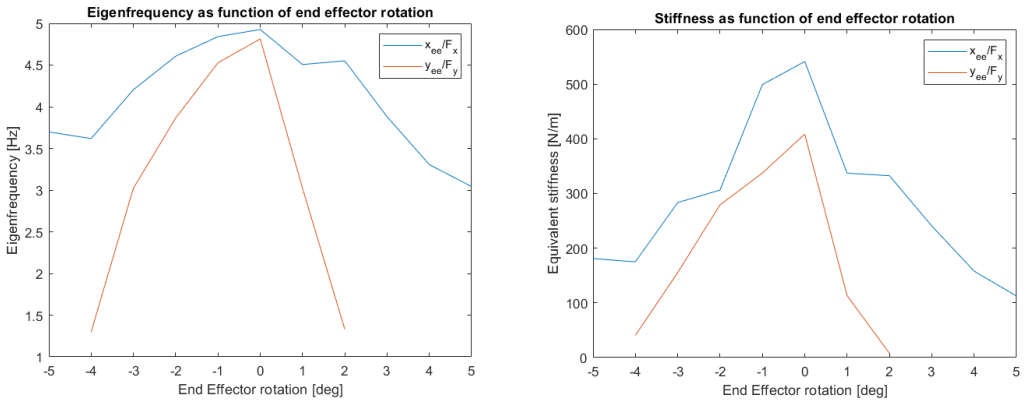

(a) First and second natural frequency

(b) Equivalent stiffness

Figure 10. Dynamic properties as functions of the end effector rotation in the neutral position.

Fig. 10 also presents the relation between y_{ee} and $f_{y,ee}$. For this relation no data is shown for an EE rotation of $-5°$, $3°$, $4°$ and $5°$ as for these rotations no natural frequency or phase shift could be recognised in the Bode plot.

This behaviour can also be found when the end effector is moved away from its neutral position without rotation. Fig. 9(b) presents the Bode diagram of the relation between y_{ee} and $f_{y,ee}$ for varying EE position and no rotation. It can be seen that the resonance peak and phase shift are lacking for most of the displacements.

The absence of the natural frequency and phase shift indicates a negative stiffness. A likely cause for this unexpected behaviour is cogging. When rotating the direct drive actuator manually it can be noticed that the rotation of the motor axle tends to stick to preferred angles. In between a negative stiffness is likely to occur from the motor rotation which is parallel to the positive stiffness of the manipulator and in this way results in a varying combined stiffness. A detailed analysis of this behaviour is left for future research.

6 CONCLUSIONS

This paper presents a first design of a planar 3-DOF 4RRR parallel manipulator with redundant actuation and compliant joints. This first prototype shows dynamic behaviour in the neutral configuration in agreement with numerical expectations. It confirms that so far the design methodology and modelling are applicable and can be used to further optimise the system. However, some unexpected behaviour has been observed for end effector positions and rotations different from the neutral configuration. Cogging of the direct drive actuators may contribute significantly to the total stiffness of the system and should be investigated in more detail in future research.

REFERENCES

[1] Berendsen, D., Sridhar, A., Aarts, R.: A compliant and redundantly actuated 2-DOF 3RRR PKM: Less is more. In: Proceedings of the 10th ECCOMAS Thematic Conference on Multibody Dynamics, Budapest University of Technology and Economics (2021) 246–256 doi:10.3311/ECCOMASMBD2021-164.

[2] Cornelissen, R., Müller, A., Aarts, R.: A compliant and redundantly actuated 2-DOF 3RRR PKM: Best of both worlds? In Kecskeméthy, A., Geu Flores, F., eds.: Multibody Dynamics 2019. Springer International Publishing, Cham (2020) 163–171 doi:10.1007/978-3-030-23132-3_20.

[3] Howell, L.L., Magleby, S.P., Olsen, B.M.: Handbook of Compliant Mechanisms. John Wiley & Sons Ltd. (2013) ISBN:978-1-119-95345-6.

[4] Soemers, H.: Design principles for precision mechanisms. T-Point Print VoF (2011) ISBN:978-90-365-3103-0.

[5] Cheng, H., Yiu, Y.K., Li, Z.: Dynamics and control of redundantly actuated parallel manipulators. IEEE/ASME Transactions on Mechatronics **8**(4) (2003) 483–491 doi:10.1109/TMECH.2003.820006.

[6] Kock, S., Schumacher, W.: A parallel x-y manipulator with actuation redundancy for high-speed and active-stiffness applications. In: Proceedings of the 1998 IEEE International Conference on Robotics and Automation. Volume 3., Leuven, Belgium (1998) 2295–2300 doi:10.1109/ROBOT.1998.680665.

[7] Liang, D., Song, Y., Sun, T., Dong, G.: Optimum design of a novel redundantly actuated parallel manipulator with multiple actuation modes for high kinematic and dynamic performance. Nonlinear Dynamics **83**(1) (2016) 631–658 doi:10.1007/s11071-015-2353-1.

[8] Müller, A., Hufnagel, T.: Model-based control of redundantly actuated parallel manipulators in redundant coordinates. Robotics and Autonomous Systems **60**(4) (2012) 563–571 doi:10.1016/j.robot.2011.11.014.

[9] Stoffels, P.: Optimization and control of a redundantly actuated 3-dof planar manipulator with flexure joints. Master's thesis, University of Twente, Enschede, The Netherlands (2021)

[10] Henein, S., Spanoudakis, P., Droz, S., Myklebust, L., Onillon, E.: Flexure pivot for aerospace mechanisms. In: 10^{th} European space mechanisms and tribology symposium, San Sebastian, Spain (2003) 285–288

[11] Farah, S., Anderson, D.G., Langer, R.: Physical and mechanical properties of PLA, and their functions in widespread applications — a comprehensive review. Advanced Drug Delivery Reviews **107** (2016) 367–392 doi:10.1016/j.addr.2016.06.012.

[12] EOS GmbH Electro Optical Systems: Fine Polyamide PA 2200 for EOSINT P. https://www.sculpteo.com/media/data/faq/pa2200-datasheet.pdf (2010) Accessed: November 2021.

[13] Woo, S.H., Kim, S.M., Kim, M.G., Yi, B.J., Kim, W.: Torque-balancing algorithm for the redundantly actuated parallel mechanism. Mechatronics **42** (2017) 41–51

[14] Jonker, J.B.: Three-dimensional beam element for pre- and post-buckling analysis of thin-walled beams in multibody systems. Multibody System Dynamics **52**(1) (2021) 59–93 doi:10.1007/s11044-021-09777-x.